

21 **Abstract**

22 It has been suggested that the uniquely high $\delta^{30}\text{Si}$ signature of North Atlantic Deep Water (NADW)
23 results from the contribution of isotopically fractionated silicic acid by mode and intermediate waters
24 that are formed in the Southern Ocean and transported to the North Atlantic within the upper limb of
25 the meridional overturning circulation (MOC). Here, we test this hypothesis in a suite of ocean general
26 circulation models (OGCMs) with widely varying MOCs and related pathways of nutrient supply to
27 the upper ocean. Despite their differing MOC pathways, all models reproduce the observation of a
28 high $\delta^{30}\text{Si}$ signature in NADW, as well showing a major or dominant (46–62%) contribution from
29 Southern Ocean mode/intermediate waters to its Si inventory. These models thus confirm that the $\delta^{30}\text{Si}$
30 signature of NADW does indeed owe its existence primarily to the large-scale transport of a distal
31 fractionation signal created in the surface Southern Ocean. However, we also find that more proximal
32 fractionation of Si upwelled to the surface within the Atlantic Ocean must also play some role,
33 contributing 20–46% of the deep Atlantic $\delta^{30}\text{Si}$ gradient. Finally, the model suite reveals
34 compensatory effects in the mechanisms contributing to the high $\delta^{30}\text{Si}$ signature of NADW, whereby
35 less export of high- $\delta^{30}\text{Si}$ mode/intermediate waters to the North Atlantic is compensated by production
36 of a high- $\delta^{30}\text{Si}$ signal during transport to the NADW formation region. This trade-off decouples the
37 $\delta^{30}\text{Si}$ signature of NADW from the pathways of deep water upwelling associated with the MOC. Thus,
38 whilst our study affirms the importance of cross-equatorial transport of Southern Ocean-sourced Si in
39 producing the unique $\delta^{30}\text{Si}$ signature of NADW, it also shows that the presence of a deep Atlantic
40 $\delta^{30}\text{Si}$ gradient does not uniquely constrain the pathways by which deep waters are returned to the
41 upper ocean.

42

43 **Keywords:** biogeochemical cycles, silicon isotopes, meridional overturning circulation

44

45 **1. Introduction**

46 *1.1. Marine Si cycling and the $\delta^{30}\text{Si}$ distribution*

47 The cycling of nutrients in the sea is determined by a complex set of interactions between biota in
48 the surface ocean and the physical circulation across a range of spatial and temporal scales. At the
49 global scale, the export of nutrients to the abyss in biogenic particles is balanced by the supply of
50 dissolved nutrients via the upwelling of nutrient-rich deep waters in the MOC (Broecker and Peng,
51 1982; Sarmiento et al., 2007). At the scale of the thermocline, nutrient distributions are determined by
52 how the location and timing of biological nutrient drawdown at the surface interacts with the
53 subduction of water masses and their gyre- to basin-scale circulation (Sarmiento et al., 2004; Palter et
54 al., 2005; Karleskind et al., 2011). These distributions in turn determine the magnitude, biogeography
55 and distribution of low-latitude primary productivity (Marinov et al., 2006; Palter et al., 2010, 2011).
56 The ocean interior distributions of nutrients thus both influence and are influenced by biological
57 productivity, and bear the imprint of the interaction between productivity and the ocean's three-
58 dimensional circulation, allowing them to be used to infer the physical and biological interactions that
59 determine marine nutrient cycling. This study takes such an approach in order to trace the influence of
60 physical-biological interactions on the large-scale transports associated with the marine cycle of
61 silicon (Si).

62 Of the ocean's photosynthesising primary producers, diatoms are the most important group for the
63 export of organic carbon from the surface ocean (e.g. Buesseler, 1998). As a result, they play a key
64 role in the biological pump, a mechanism by which the ocean modulates atmospheric pCO_2 (Hain et
65 al., 2014a). Whilst their opaline cell wall, or frustule, provides diatoms protection from predators
66 (Smetacek, 1999) and is less energy-intensive to produce than an organic cell wall (Raven, 1983), it
67 also makes them vitally dependent on the presence of Si dissolved in seawater. The boom-bust
68 behaviour of diatom populations that leads to their importance for carbon export also means that
69 diatoms are very efficient exporters of Si to depth (Brzezinski et al., 2003), such that they are the main
70 driver of marine Si cycling (Tréguer and De La Rocha, 2013). Diatom uptake of Si discriminates
71 between its isotopes, with lighter Si isotopes being preferentially incorporated into the frustule (De La
72 Rocha et al., 1997; Sutton et al., 2013), leaving the residual Si in seawater enriched in heavier Si

73 isotopes. Diatom Si uptake at the ocean's surface thus produces a signal of biological cycling in the
74 stable isotope composition of seawater Si (expressed in the standard delta notation as $\delta^{30}\text{Si}$), which can
75 be used as a tracer of the marine Si cycle (e.g. Cardinal et al., 2005; Reynolds et al., 2006; Beucher et
76 al., 2008; de Souza et al., 2012a; Grasse et al., 2013). For instance, diatom uptake in the surface
77 Southern Ocean produces elevated $\delta^{30}\text{Si}$ in the deep winter mixed layers from which the Southern
78 Ocean mode/intermediate water masses Subantarctic Mode Water (SAMW) and Antarctic
79 Intermediate Water (AAIW) are ventilated (Fripiat et al., 2011). This isotopic signal is transported into
80 the subtropical interior by the spreading of these water masses from their formation regions (de Souza
81 et al., 2012b).

82 The clearest large-scale signal in the marine $\delta^{30}\text{Si}$ distribution is the $\delta^{30}\text{Si}$ gradient in the deep
83 Atlantic Ocean (Fig. 1a; de Souza et al., 2012a; Brzezinski and Jones, 2015), with a systematic trend
84 from high $\delta^{30}\text{Si}$ values in deep waters of the Si-poor North Atlantic, influenced by NADW, to lower
85 values towards the Si-richer south, influenced by Antarctic Bottom Water (AABW). This coherent
86 gradient is related to the quasi-conservative mixing of Si between these two water masses (Broecker et
87 al., 1991), as reflected by the systematics (Fig. 1a) and water-column distribution (Fig. 1b) of $\delta^{30}\text{Si}$ in
88 the Atlantic, both of which indicate water-mass control on the $\delta^{30}\text{Si}$ distribution. de Souza et al.
89 (2012a) suggested that the high $\delta^{30}\text{Si}$ value of NADW ultimately results from the creation of a high-
90 $\delta^{30}\text{Si}$ signal by diatom Si uptake in the surface Southern Ocean, a signal that is transported to the
91 North Atlantic by SAMW/AAIW in the upper limb of the MOC. This mechanism has since been
92 invoked to explain the isotope distributions of other biogeochemically-cycled elements, such as
93 cadmium (e.g. Abouchami et al., 2014).

94 Such a Southern-Ocean-focused mechanism is consistent with burgeoning evidence that the
95 dominant MOC pathway by which dense and nutrient-rich deep waters are brought to the surface is the
96 wind-driven upwelling in the Southern Ocean (Toggweiler and Samuels, 1993; Sarmiento et al., 2004;
97 Lumpkin and Speer, 2007; Marshall and Speer, 2012; Morrison et al., 2015), contrary to the canonical
98 view of upwelling through the low-latitude thermocline (Robinson and Stommel, 1959; Broecker and
99 Peng, 1982). However, some recent observationally-based estimates of global overturning indicate a
100 significant role of low-latitude upwelling in closing the MOC (Talley et al., 2003; Talley, 2008). By

101 using numerical ocean models to examine the relationship between the NADW $\delta^{30}\text{Si}$ signature and the
102 pathways by which Si is transported by the MOC, this study assesses de Souza et al.'s (2012a)
103 hypothesis of large-scale controls on the Atlantic $\delta^{30}\text{Si}$ distribution, whilst also considering the
104 constraints placed by these observations on pathways of upwelling associated with the MOC.

105 *1.2. Support for a Southern Ocean control*

106 Support for a Southern Ocean control on the NADW $\delta^{30}\text{Si}$ signature is provided by the model
107 CYCLOPS, an ocean box model originally developed by Keir (1988) that has been modified to
108 explicitly represent the physical and biogeochemical zonation of the surface Southern Ocean (Fig. 2a;
109 Robinson et al., 2005; Hain et al., 2014b). A representation of the marine cycling of Si and its isotopes
110 (see Supplementary Information) allows an assessment of the leading-order sensitivities of the large-
111 scale $\delta^{30}\text{Si}$ distribution. As shown in Fig. 2b, the observed deep Atlantic Si concentration gradient
112 ($\sim 110 \mu\text{M}$) can be reproduced by simultaneously varying the length-scale defining the dissolution of
113 opal export (which determines the partitioning of opal dissolution between the intermediate and deep
114 ocean) and the degree of Si drawdown in the Subantarctic Zone (SAZ), from where the model's
115 Southern Ocean mode/intermediate waters are ventilated. In contrast, the gradient in $\delta^{30}\text{Si}$ between
116 NADW and the deep Southern Ocean is mostly insensitive to the opal dissolution length-scale, but
117 varies systematically with Si drawdown in the SAZ, disappearing when the Si concentration in the
118 SAZ is forced to zero, so as not to leave any residual high- $\delta^{30}\text{Si}$ in the SAZ surface (Fig. 2b). Under
119 these conditions, the model's advective pathway of Si supply from the surface Southern Ocean to the
120 high-latitude North Atlantic via mode/intermediate waters has been entirely eliminated, such that Si
121 can reach the North Atlantic solely via diffusive upward supply from the low-latitude deep ocean. This
122 sensitivity of the Atlantic $\delta^{30}\text{Si}$ gradient to Si supply by mode/intermediate waters supports the
123 hypothesis that it results from the cross-equatorial transport of a partial Si consumption signal from the
124 surface Southern Ocean. In the following, we further test this hypothesis by explicitly tracing the
125 origins of Si supplied to the North Atlantic by the large-scale ocean circulation in a suite of OGCMs in
126 which the pathways of deep water upwelling associated with the MOC are systematically varied.

127 *1.3. A theoretical framework*

128 Gnanadesikan's (1999; hereafter G99) analytical model of the volume balance of the oceanic
129 pycnocline (Fig. 3a) provides the conceptual basis for the OGCM suite presented in this study. This
130 model shows that the depth D of the pycnocline, separating the buoyant waters of the upper ocean
131 from the dense waters of the deep, results from the balance between four key processes that add or
132 remove buoyant water from the upper ocean. These processes are (i) the formation of deep water in the
133 North Atlantic (T_n in Fig. 3a), the balance between (ii) wind-driven upwelling and northward Ekman
134 transport in the Southern Ocean (T_w) and (iii) southward eddy-induced advection of light waters (T_e),
135 and (iv) low-latitude upwelling through the thermocline (T_u). There are two pathways by which
136 volume lost from the upper ocean during NADW formation can be replaced: (a) downward heat
137 transport driven by diapycnal mixing lightens dense waters, leading to an upwelling flux through the
138 thermocline; (b) Ekman divergence in the Southern Ocean drives the adiabatic upwelling of deep
139 waters, which are converted to lighter waters at the surface. G99 showed that the partitioning of
140 upwelling between these two pathways depends on diapycnal mixing and the advective effects of
141 eddies, represented by the diapycnal and isopycnal eddy diffusivities (κ_v and A_l) respectively. When
142 these diffusivities are small, both low-latitude upwelling T_u and the eddy return flow T_e compensating
143 northward Ekman transport T_w are minimal, such that deep upwelling (and the associated nutrient
144 supply) is driven by Ekman divergence in the surface Southern Ocean T_w (Fig. 3a). If, on the other
145 hand, A_l is large enough that the southward advective eddy transport in the Southern Ocean largely
146 compensates northward Ekman transport (i.e. if the net flux $T_w - T_e$ is small), most upwelling takes
147 place at low latitudes (T_u). This simultaneously requires high κ_v in order to maintain the observed
148 depth of the pycnocline against a large upwelling flux. This simple model thus makes an important
149 point: the pathway by which dissolved nutrients stored in the deep ocean return to the surface depends
150 on the vigorousness of turbulent mixing across and along density surfaces. By varying both these
151 parameters simultaneously in a numerical ocean model, we can produce widely varying pathways of
152 upwelling whilst maintaining the observed depth of the ocean's pycnocline. This study utilises three
153 variants of an OGCM with differing MOC pathways in order to systematically examine the
154 relationship between the $\delta^{30}\text{Si}$ signature of NADW and large-scale Si transport.

155

156 2. Methods

157 2.1. Model description and setup

158 The physical ocean model used is the Modular Ocean Model 3.0 (MOM3; Pacanowski and Griffies,
159 1999), run at $3.75^\circ \times 4.5^\circ$ horizontal resolution with 24 vertical levels. This primitive-equation OGCM
160 forms the basis of a model suite in which the values of diapycnal and isopycnal diffusivity are
161 systematically varied according to the theory of G99, so as to produce varying MOC pathways. This
162 suite is described in detail by Gnanadesikan et al. (2002, 2004, 2007) and Palter et al. (2010). In this
163 study, we employ model variants LL, HH and P2A, whose key variables are summarized in Table S1.
164 Model variant LL is a version of MOM3 in which both diapycnal and isopycnal eddy diffusivities
165 have low values. In LL, κ_v in the pycnocline is 1.5×10^{-5} m²/s, similar to values inferred from direct
166 tracer release experiments (Ledwell et al., 1993, 1998), increasing to 1.3×10^{-4} m²/s at depth with a
167 hyperbolic tangent transition at 2500 m. Isopycnal diffusivity A_I , which is also the coefficient used in
168 the models' Gent–McWilliams parameterization of eddy thickness diffusion (Gent et al., 1995), has a
169 constant value of 1000 m²/s in LL. In model variant HH, in contrast, both κ_v and A_I have high values:
170 at 6×10^{-5} m²/s, pycnocline κ_v is four times higher than in LL, whilst the A_I of 2000 m²/s is twice as
171 large as in LL. Finally, model variant P2A conforms to observational constraints of low pycnocline
172 diffusivity (and thus has a pycnocline κ_v of 1.5×10^{-5} m²/s and A_I of 1000 m²/s, as in LL), but simulates
173 increased diapycnal mixing in the Southern Ocean, motivated by observations of high internal wave
174 activity there (Polzin et al., 1997). In addition to a number of specific changes relative to LL as listed
175 in Table S1 (and discussed by de Souza et al., 2014), P2A is forced by the ECMWF atmospheric
176 reanalysis of Trenberth et al. (1989), which imposes higher wind stresses over the Southern Ocean
177 than the reanalysis that forces LL and HH (Hellerman and Rosenstein, 1983).

178 The physical models are coupled to the nutrient-restoring biogeochemical model of Jin et al. (2006),
179 modified by de Souza et al. (2014) to include Si isotopes. As discussed therein, the model simulates
180 isotope fractionation during Si uptake in the surface ocean, but does not fractionate Si isotopes during
181 opal dissolution (Demarest et al., 2009; Wetzel et al., 2014; for a detailed discussion of this issue see
182 de Souza et al., 2014). Further diagnostics added for this study (Section 2.2) allow us to trace Si
183 originating from four high-latitude source regions in the models.

184 The simulations are initialized to steady-state physical conditions and distributions of Si and $\delta^{30}\text{Si}$
185 from a 5000-yr spin-up simulation for each model variant. The fractional contribution of each of the
186 four source regions (Section 2.2) to the Si inventory is initialized to a globally constant value of 25%,
187 and the simulations run forward for 2000 model years, by which time the Si source tracer distributions
188 achieve equilibrium. Targets for surface nutrient restoring are derived from the objectively-analysed
189 monthly climatologies of World Ocean Atlas 2009 (WOA09; Garcia et al., 2010). Results of the
190 simulations are presented as averages over the last 20 years of the simulations. We also present the
191 models' equilibrium (pre-bomb) radiocarbon distributions ($\Delta^{14}\text{C}$; Matsumoto et al., 2004) as 10-year
192 means.

193 2.2. Si source tagging scheme

194 In order to study the large-scale Si dynamics and transport in the model variants, we explicitly trace
195 four sources of Si, using the method of Palter et al. (2010). As defined in Fig. 4, we tag and trace Si
196 sourced from (a) the region of SAMW formation (*SAMW*), (b) the region of AAIW formation (*AAIW*),
197 (c) the deep Southern Ocean (*DEEP*), and (d) the subpolar North Pacific Ocean (*NPAC*). At every
198 model time step, Si within a defined source region is 'tagged' with the corresponding source identity.
199 For example, AAIW-derived Si is tagged between the $\sigma_\theta = 27.1$ and $\sigma_\theta = 27.4$ isopycnals south of
200 where the $\sigma_\theta = 26.5$ isopycnal shoals to 200m (see Fig. 4). Si tagged in this manner is transported
201 away from its source region by the circulation, and retains its source identity as it cycles through the
202 low latitude ocean and into the North Atlantic, our region of interest. Once acquired, source identity is
203 only destroyed when Si enters another source region: e.g., AAIW-derived Si flowing northward in the
204 surface Southern Ocean will lose its AAIW identity and be tagged as SAMW-sourced Si once it
205 crosses the instantaneous outcrop of the $\sigma_\theta = 27.1$ isopycnal. The sum of all four source tracers equals
206 the total pool of Si, allowing us to trace the fractional contribution of the source regions to the local Si
207 inventory at any point in the model. In the following, we refer to Si that has been tagged with a
208 particular source identity as being 'sourced' or 'derived' from that region (e.g. 'SAMW-derived').

209

210 3. Results

211 *3.1. MOC pathways, Si and $\delta^{30}\text{Si}$ distributions*

212 We begin by describing the upwelling pathways of the three model variants. Figure 3b shows the
213 zonally-averaged northward meridional volume transport above the $\sigma_\theta = 27.4$ isopycnal, which lies at
214 a depth of 800–1000 m at low latitudes in all models. An increase in horizontal transport implies
215 upwelling of water across this density surface, into the upper ocean. Thus, the differing latitudinal
216 evolution of this transport in the models reflects their differing MOC pathways. The constancy of
217 P2A’s meridional transport north of $\sim 50^\circ\text{S}$ shows that this model achieves most of its upwelling at
218 high southern latitudes (Fig. 3b). This Southern Ocean upwelling pathway is expected from G99 (Fig.
219 3a), given the low isopycnal and diapycnal diffusivities and the strong winds over the Southern Ocean
220 (Table S1): P2A not only restricts T_u through limited low-latitude diapycnal mixing and T_e through
221 low isopycnal diffusivity, but also has high T_w as a result of stronger Ekman transport in the Southern
222 Ocean. In contrast, volume transport in HH increases over a wide latitudinal band from $\sim 50^\circ\text{S}$ to
223 $\sim 30^\circ\text{N}$, reflecting low-latitude upwelling. The importance of low-latitude transport (T_u) for the
224 overturning is expected from G99, given HH’s high diffusivities and weaker Southern Ocean winds.
225 Model variant LL is intermediate between these two extremes, since southern upwelling extends
226 further north than in P2A, but limited low-latitude upwelling is implied by the constancy of meridional
227 volume transport north of $\sim 30^\circ\text{S}$. The overturning pathways simulated by LL and P2A are more
228 consistent with estimates from inverse models (Lumpkin and Speer, 2007) and the emerging view of
229 ocean overturning (Marshall and Speer, 2012; Talley, 2013), although LL’s ventilation of the deep
230 Southern and Pacific Oceans is too sluggish to accurately reproduce the $\Delta^{14}\text{C}$ distribution (Matsumoto
231 et al., 2004).

232 When combined with their shared biogeochemical model, which restores surface Si concentrations
233 towards observations, the circulation fields of the three models produce interior Si distributions that
234 reproduce the large-scale structure to the observed distribution, but also show differences both from
235 the observations and from each other. Figure 5 compares the models’ average Atlantic Si distribution
236 in the uppermost 2400m with WOA09 (see Fig. S3 for zonal averages). As in the observations, all
237 models exhibit a southward propagating tongue of low-Si NADW at mid-depth, and an intermediate-
238 depth tongue of elevated Si extending northwards from the Southern Ocean. However, in all model

239 variants, the low-Si tongue is too shallow, with a core at ~1600 m rather than ~1800m as in the
 240 observations. This is because North Atlantic convection in the models produces a water mass that is
 241 too light and thus descends to shallower depths than observed. As a result, the models' Si-rich AABW
 242 extends too far north, and upward diapycnal mixing of Si from this water mass leads to the elevated Si
 243 concentrations seen below ~2200m in all model variants. All models also overestimate Si in the
 244 northward-penetrating intermediate-depth tongue, a feature that is more pronounced in P2A and HH
 245 than in LL. The Si distribution of HH is least similar to the observations: the southward- and
 246 northward-propagating advective signals are much less clearly defined in this model than in LL or
 247 P2A, due to high interior diapycnal mixing. Model HH also strongly underestimates Si concentrations
 248 in the deep Southern Ocean relative to observations.

249 Despite these differences in the Si distribution between models, they display similar skill at
 250 reproducing the interior Atlantic $\delta^{30}\text{Si}$ distribution, especially in terms of its isotope systematics: as
 251 shown by Fig. 1a, all three models reproduce the near-linear $\delta^{30}\text{Si}-1/\text{Si}$ relationship observed in the
 252 deep Atlantic Ocean, simulate a similar range of $\delta^{30}\text{Si}$ variation in Atlantic deep waters, and reproduce
 253 the observation of elevated $\delta^{30}\text{Si}$ in the Si-poor deep North Atlantic. We will discuss the reasons for
 254 these similarities in Section 4. For now, bearing the differences in the Si distribution of the three
 255 models in mind, in the following we discuss the Si source tracer distributions in terms of their
 256 *fractional* contribution to the total Si inventory, $f(i) = [\text{Si}]_{\text{source} = i} / \sum_j [\text{Si}]_{\text{source} = j}$.

257 3.2. Si source tracer distributions

258 By examining the steady-state distributions of the Si source tracer contributions $f(i)$, we can study
 259 how Si from the four source regions spreads through the ocean to eventually contribute to the NADW
 260 Si inventory. We illustrate the influence of the models' differing MOC pathways on large-scale Si
 261 transport by examining the contribution of each source region to the Si inventory of the thermocline,
 262 which we define as the volume of water above the $\sigma_\theta = 26.8$ isopycnal.

263 The two sources of Si above the $\sigma_\theta = 26.8$ isopycnal, SAMW and NPAC, exhibit their maximal
 264 contributions to the thermocline Si inventory close to their source regions, from where Si is directly
 265 introduced into the thermocline (Fig. 6). The locus of maximum fraction of SAMW-derived Si,

266 $f(\text{SAMW})$, follows typical SAMW ventilation pathways (Sallée et al., 2010), extending anti-clockwise
267 into the subtropics from the southern outcrop (Fig. 6a). NPAC-sourced Si enters the North Pacific
268 thermocline from the north (Fig. 6d), and is transported into the Indian Ocean via the Indonesian
269 Throughflow, although virtually none enters the Atlantic via the warm-water pathway (Gordon, 1986)
270 without first entering the SAMW source region and losing its NPAC identity. NPAC-derived Si also
271 flows northward through Bering Strait, contributing considerably to the Si inventory of the Arctic
272 Ocean above $\sigma_\theta = 26.8$.

273 Silicon sourced from below the $\sigma_\theta = 26.8$ isopycnal (AAIW and DEEP) exhibits rather different
274 thermocline distributions, since it can enter the thermocline only via interior diapycnal fluxes across
275 this isopycnal. Thus, the contribution of AAIW- and DEEP-sourced Si increases towards the
276 subtropics and tropics, as deeper-lying Si is transported upwards (Fig. 6b,c). In concordance with the
277 models' differing MOC pathways, the contribution of DEEP-sourced Si to the thermocline inventory
278 is highest in the diffusive model HH, and is lowest in the more adiabatic P2A, whose thermocline is
279 also more vigorously ventilated along isopycnals from the south due to higher wind stress over the
280 Southern Ocean. The contribution of DEEP-sourced Si to the thermocline inventory is 1.3–1.6 times
281 higher in HH than in LL or P2A in the low-latitude Indian and Pacific Oceans, and even higher in the
282 Atlantic, where it can be more than twice as large in HH than in P2A (Fig. 6c). Complementarily, high
283 contributions of SAMW- and AAIW-derived Si penetrate further northward in LL and P2A than in
284 HH: high contributions of SAMW-derived Si extend well into the North Atlantic in LL and P2A, such
285 that $f(\text{SAMW})$ is 1.3–1.7 times higher in the tropical Atlantic thermocline of these models than in HH
286 (Fig. 6a). Additionally, the fraction of AAIW-derived Si in the Atlantic thermocline increases steadily
287 towards the north in LL and P2A but not in HH, such that in the North Atlantic subtropics, $f(\text{AAIW})$ in
288 P2A and LL is 1.2–1.5 times higher than in HH (Fig. 6b). In all three models, however, SAMW- and
289 AAIW-sourced Si together contribute at least half the Si inventory of the North Atlantic thermocline.

290 3.3. Diapycnal Si redistribution in the Atlantic Ocean

291 The consequences of northward transport of SAMW- and AAIW-derived Si for the source
292 composition of NADW are illustrated by Fig. 7, which shows the average source tracer contributions
293 $f(i)$ in the uppermost 2400m of the Atlantic Ocean (see Fig. S4 for zonal averages). Only SAMW-

294 derived Si spreads northwards at the surface, whilst Si from other source regions enters the Atlantic
295 within the interior. Diapycnal processes and biological cycling disperse Si from all four source regions
296 through the water column, e.g. the upward transport of DEEP-sourced Si into the thermocline, seen
297 most strongly in HH (Fig. 7c). However, diapycnal Si redistribution is reflected most dramatically by
298 the two source tracers that are tagged in the upper ocean according to density criteria, i.e. SAMW and
299 AAIW. The downward penetration of Si from these sources is greatest in the North Atlantic north of
300 40°N (Fig. 7a,b). A tongue of elevated $f(\text{SAMW})$ and $f(\text{AAIW})$ propagates southwards from these
301 high latitudes at about 1500-1600m, at densities significantly higher than those at which these tracers
302 are originally tagged (Fig. S5). This mid-depth tongue is the signal of NADW (Fig. 5), and reflects the
303 diapycnal transfer of Si sourced from the shallow Southern Ocean to deep water densities, due to
304 buoyancy loss in the subpolar North Atlantic, the Nordic Seas and the Arctic Ocean. The incorporation
305 of SAMW- and AAIW-derived Si into NADW takes place in all three model variants, although their
306 importance for its Si inventory varies, due to the differing extent of their transport to the shallow North
307 Atlantic. All three models also exhibit a deep (~1800m) tongue of NPAC-sourced Si extending
308 southwards from the subpolar North Atlantic (Fig. 7d). This is Si that has been transported from the
309 North Pacific via the Arctic Ocean, entering the North Atlantic through the models' representation of
310 the Nordic Sea overflows.

311

312 **4. Discussion**

313 The Si source tracer distributions reveal the pathways of large-scale Si transport and diapycnal
314 redistribution in the Atlantic Ocean. In the following, we focus on NADW flowing southward from
315 the subpolar North Atlantic, in order to elucidate the processes responsible for its unique $\delta^{30}\text{Si}$
316 signature.

317 *4.1. The isotopic signatures and source composition of NADW*

318 As indicated by the simulated Atlantic $\delta^{30}\text{Si}$ systematics (Fig. 1a), which show elevated $\delta^{30}\text{Si}$ values
319 associated with Si-poor waters of the deep North Atlantic, NADW appears prominently in the
320 simulated $\delta^{30}\text{Si}$ distribution as a high- $\delta^{30}\text{Si}$ tongue along the western boundary of the mid-depth North
321 Atlantic in all three models (Fig. 8a). The basin-scale structure of the simulated $\delta^{30}\text{Si}$ distributions is

322 broadly consistent with observations of elevated $\delta^{30}\text{Si}$ values ranging from +1.7 to +1.9‰ in the
323 western mid-depth North Atlantic (Fig. 1b; de Souza et al., 2012a; Brzezinski and Jones, 2015). Whilst
324 the less diffusive models P2A and LL reproduce the absolute $\delta^{30}\text{Si}$ values in NADW better than the
325 diffusive model HH (Figs. 8a,c), all three models reproduce the $\delta^{30}\text{Si}$ systematics of the deep Atlantic
326 with similar fidelity (Fig. 1a), although P2A simulates higher $\delta^{30}\text{Si}$ values in the subpolar North
327 Atlantic than LL or HH. It is interesting to note that the models reproduce the observed near-linear
328 $\delta^{30}\text{Si}$ systematics despite the fact that they do not simulate Si isotope fractionation during opal
329 dissolution. This contrasts somewhat with the recent study by Holzer and Brzezinski (2015), who
330 found that including this process improved the linearity of their model's Atlantic $\delta^{30}\text{Si}$ systematics by
331 increasing $\delta^{30}\text{Si}$ in the Si-richest Southern Ocean deep waters. Our results and theirs do, however,
332 agree in suggesting that fractionation during opal dissolution is not a major driver of the deep Atlantic
333 $\delta^{30}\text{Si}$ systematics.

334 Depth sections across $\sim 43^\circ\text{N}$ reveal the isotopic signal of NADW flowing around the Grand Banks
335 as a well-ventilated water mass: this freshly-ventilated NADW bears a $\Delta^{14}\text{C}$ maximum (Fig. 8b) and is
336 recognizable in the $\delta^{30}\text{Si}$ distribution by its elevated $\delta^{30}\text{Si}$ signature (Fig. 8c) in all models. These
337 isotopic distributions are closely mimicked by the fraction of Si sourced from SAMW and AAIW,
338 $f(\text{SAMW}+\text{AAIW})$ (Fig. 8d). The fractional contribution of SAMW- and AAIW-derived Si is highest
339 above the 27.4 isopycnal, in waters flowing towards the high-latitude North Atlantic in the upper limb
340 of the MOC. However, in each model, there is a secondary $f(\text{SAMW}+\text{AAIW})$ maximum at mid-depth,
341 coincident with the $\delta^{30}\text{Si}$ and $\Delta^{14}\text{C}$ signals of NADW. The fraction of NPAC-derived Si also shows a
342 maximum within this volume, but does not exceed 10% (Fig. S6d). Conversely, DEEP-sourced Si is at
343 its minimum within the freshly-ventilated NADW core (Fig. S6c). Thus, irrespective of the large-scale
344 circulation of the models, there is a clear spatial correlation between the maximum contribution of
345 SAMW- and AAIW-derived Si to NADW and the elevated $\delta^{30}\text{Si}$ signature observed in the most
346 recently ventilated deep waters (Figs. 8c,d and S7). We can quantify this relationship by calculating
347 the contributions of the source regions to the Si inventory of freshly-ventilated NADW.

348 Recently ventilated NADW exhibits clear signals of gas exchange with the atmosphere in the
349 models' radiocarbon and oxygen distributions (Figs. 8b, S1 and S2). We exploit these signals to define
350 a volume of freshly-ventilated NADW that extends from the shallow subpolar North Atlantic (>500m
351 water depth) to the equator along the western Atlantic boundary (Table 1; see also the Supplementary
352 Information). This allows us to calculate the integrated Si inventory of this volume and partition it
353 according to source region (Table 1). In all three model variants, SAMW and AAIW together
354 contribute a major or dominant fraction of the Si inventory, ranging from 46% in HH to 62% in P2A.
355 The importance of DEEP-sourced Si varies inversely with this contribution, whilst NPAC-derived Si
356 is of minor importance (5–9%) in all models.

357 The $\delta^{30}\text{Si}$ signature of the freshly-ventilated NADW volume rises systematically with the increase in
358 $f(\text{SAMW}+\text{AAIW})$ from HH to P2A, and ranges from +1.50‰ in HH to +1.74‰ in P2A (Table 1).
359 Thus, not only is there a clear spatial correlation between elevated values of $f(\text{SAMW}+\text{AAIW})$ and
360 $\delta^{30}\text{Si}$ *within* each model (Fig. S7), but also systematic co-variation *between* models: the greater the
361 SAMW/AAIW contribution to NADW, the higher its $\delta^{30}\text{Si}$ value. Together, these correlations strongly
362 suggest that cross-equatorial transport of Si that has been isotopically fractionated in the surface
363 Southern Ocean is instrumental in producing the high $\delta^{30}\text{Si}$ signature of NADW.

364 4.2. Distal and proximal fractionation controls on the NADW $\delta^{30}\text{Si}$ signature

365 The elevated $\delta^{30}\text{Si}$ signal of NADW is reproduced by all three models, despite their widely varying
366 MOC configurations. Whilst the analysis above indicates that this signal derives from the contribution
367 of SAMW/AAIW to NADW's Si inventory, we must also consider two additional factors that can
368 produce differences in the NADW $\delta^{30}\text{Si}$ signature between model variants. These are: (a) the isotopic
369 composition of Si exported from each source region, and (b) Si isotope fractionation at the ocean's
370 surface during transport from the source regions to the North Atlantic. In other words, the NADW
371 $\delta^{30}\text{Si}$ signature can be conceived of as resulting from a combination of the *conservative* transport of
372 isotope signatures from distal source regions, and the *non-conservative* alteration of these isotope
373 signatures en route. We can separate the effects of these two factors with a simple isotope mixing
374 calculation, allowing us to assess the extent to which the NADW $\delta^{30}\text{Si}$ signature is controlled by the

375 conservative transport of distal isotopic signals. We calculate the isotopic composition of Si within
 376 each source region (Table 1) as an estimate of the distal isotopic signals being exported towards the
 377 North Atlantic. Based on these values and the source tracer contributions at each model grid point, we
 378 can then calculate the $\delta^{30}\text{Si}$ distribution that would result simply from the spreading of these
 379 endmember $\delta^{30}\text{Si}$ signatures:

$$380 \quad \delta^{30}\text{Si}_{distal} = \sum_i f(i) \cdot \delta^{30}\text{Si}_{i,source} \quad (\text{Eqn. 1})$$

381 where $f(i)$ is the local fractional contribution of the source i , and $\delta^{30}\text{Si}_{i,source}$ is the isotopic
 382 composition in the source region i . We hasten to note that this approach makes the simplifying
 383 assumption that Si supplied from each source region has a uniform $\delta^{30}\text{Si}$ value, which is not the case.
 384 However, as we show below, it nonetheless serves to provide us with a useful estimate of the influence
 385 of the large-scale transport of isotope signals.

386 The meridional sections in Fig. 9 compare the simulated Atlantic $\delta^{30}\text{Si}$ distribution at 25°W (Fig.
 387 9a) with the $\delta^{30}\text{Si}_{distal}$ distribution (Fig. 9b). It can be seen that in all three model variants, considerable
 388 large-scale interior Atlantic $\delta^{30}\text{Si}$ variability, including an elevated NADW $\delta^{30}\text{Si}$ signature, is
 389 predicted to result simply from the propagation of distal source-region $\delta^{30}\text{Si}$ signals. Furthermore, as
 390 shown by the close correlation between the two fields (Fig. 9d), the structure of the $\delta^{30}\text{Si}_{distal}$
 391 distribution bears a strong resemblance to the simulated $\delta^{30}\text{Si}$ field. These results indicate that the
 392 long-range transport of isotope signals plays a significant role in determining the basin-scale $\delta^{30}\text{Si}$
 393 distribution. However, in all cases the range in $\delta^{30}\text{Si}_{distal}$ is muted in comparison to the simulated field
 394 (slopes < 1 in Fig. 9d), with $\delta^{30}\text{Si}_{distal}$ values generally lower than simulated values in the upper ocean
 395 (Fig. 9c). This is reflected in the $\delta^{30}\text{Si}_{distal}$ signature of the freshly-ventilated NADW volume, which
 396 underestimates the simulated $\delta^{30}\text{Si}$ value by 0.13–0.22‰ (Table 1).

397 Two reasons for the mismatch between $\delta^{30}\text{Si}_{distal}$ and simulated $\delta^{30}\text{Si}$ become clear upon closer
 398 inspection of Fig. 9. Firstly, the assumption of uniform source $\delta^{30}\text{Si}$ values in Eqn. 1 ignores the
 399 significant isotopic variability within each source region. This simplification results, for example, in
 400 the northward propagation of too-low $\delta^{30}\text{Si}_{distal}$ values from the Southern Ocean just below the $\sigma_\theta =$

401 27.4 isopycnal in all models, reflected by the bolus of elevated mismatch at this location in all models
402 (Fig. 9c). Secondly, a clear difference between $\delta^{30}\text{Si}$ and $\delta^{30}\text{Si}_{distal}$ is observed in the near-surface
403 ocean, where the simulated $\delta^{30}\text{Si}$ field exhibits high values throughout the low latitudes and in the
404 subpolar North Atlantic (Fig. 9a), whilst $\delta^{30}\text{Si}_{distal}$ values in the uppermost 500m decrease considerably
405 from the southern tropics northwards (Fig. 9b). This change is seen mostly clearly at the level of
406 SAMW in all models (Fig. 9c), where the sign of mismatch between the two fields changes from
407 negative ($\delta^{30}\text{Si}_{distal} > \delta^{30}\text{Si}$) to positive ($\delta^{30}\text{Si} > \delta^{30}\text{Si}_{distal}$) towards the north. The decoupling of $\delta^{30}\text{Si}_{distal}$
408 from $\delta^{30}\text{Si}$ during northward transport in the upper ocean is the result of two opposing tendencies. A
409 decrease $\delta^{30}\text{Si}_{distal}$ is driven by the upward transport of AAIW- and DEEP-sourced Si in the low-
410 latitude ocean (Figs. 7 and 8), pools that have significantly lower $\delta^{30}\text{Si}$ values than SAMW-sourced Si
411 (Table 1). In contrast, an elevation of simulated $\delta^{30}\text{Si}$ values in the upper ocean results from isotope
412 fractionation during Si utilisation in the low latitude ocean and the subpolar North Atlantic. This
413 fractionation directly affects $\delta^{30}\text{Si}$ values in the surface ocean, but also more indirectly elevates near-
414 surface $\delta^{30}\text{Si}$ via the subduction of a high- $\delta^{30}\text{Si}$ signal into the subtropical North Atlantic thermocline.
415 Thus, some fraction of the difference between the $\delta^{30}\text{Si}$ and $\delta^{30}\text{Si}_{distal}$ fields results from the isotope
416 fractionation of Si within the Atlantic Ocean.

417 This result implies that the elevated NADW $\delta^{30}\text{Si}$ signature simulated by the models is not simply
418 the result of distal fractionation in the surface Southern Ocean, but also reflects more proximal isotope
419 fractionation as Si is transported towards the NADW formation region in the upper limb of the MOC,
420 i.e. the *non-conservative* effect discussed above. The offset between the $\delta^{30}\text{Si}$ and $\delta^{30}\text{Si}_{distal}$ fields is
421 much smaller at the depth of NADW than in the upper ocean (Fig. 9a,b), showing that the signal of
422 proximal fractionation is damped during NADW formation. This is due to the importance of Si-richer
423 subsurface waters, whose Si inventory is not exposed to isotope fractionation in the surface, in
424 determining the NADW $\delta^{30}\text{Si}$ value (cf. Sigman et al., 2000).

425 Due to the uncertainty introduced into our calculation of $\delta^{30}\text{Si}_{distal}$ by the assumption of constant
426 source region $\delta^{30}\text{Si}$ signatures, we can only provide an estimate of the extent of the proximal
427 modulation of distal isotope signals. A useful metric for this estimation is the deep Atlantic $\delta^{30}\text{Si}$

428 gradient, i.e. the difference between the $\delta^{30}\text{Si}$ values of NADW and AABW. The three model variants
429 produce Atlantic deep water $\delta^{30}\text{Si}$ differences of varying strength, ranging from 0.31‰ in HH to
430 0.63‰ in P2A (Table 1), compared to an observed difference of \sim 0.5‰ (de Souza et al., 2012a). By
431 assessing what proportion of this basin-scale $\delta^{30}\text{Si}$ difference is explained by the $\delta^{30}\text{Si}_{\text{distal}}$ signature of
432 NADW, we can estimate the fraction that results simply from the propagation of source-region $\delta^{30}\text{Si}$
433 signatures. The results shown in Table 1 reveal that this conservative effect explains 54% to 80% of
434 the deep Atlantic $\delta^{30}\text{Si}$ gradient. Our simulations thus indicate that the high $\delta^{30}\text{Si}$ value of NADW, and
435 indeed the basin-scale $\delta^{30}\text{Si}$ distribution, is largely governed by the transport of distal surface Southern
436 Ocean isotope signatures to the North Atlantic in SAMW and AAIW, as postulated by de Souza et al.
437 (2012a).

438 *4.3. Compensatory mechanisms in the Atlantic $\delta^{30}\text{Si}$ systematics*

439 The above discussion of the distal and proximal controls on the $\delta^{30}\text{Si}$ distribution also helps
440 elucidate the mechanisms by which the models all produce an elevated NADW $\delta^{30}\text{Si}$ signal, despite
441 differing pathways of deep water upwelling. The importance of the cross-equatorial transport of distal
442 isotopic signals in producing the Atlantic $\delta^{30}\text{Si}$ gradient differs between the models, and is least in the
443 highly diffusive model HH, which upwells more interior Si to the surface in the low latitudes (Table
444 1). This relationship suggests that there are compensatory mechanisms at play in the models' Atlantic
445 $\delta^{30}\text{Si}$ systematics: the more diffusive model HH advects less fractionated Si to the North Atlantic from
446 the surface Southern Ocean (Figs. 6–8), but produces a high- $\delta^{30}\text{Si}$ signal more proximally through
447 fractionation of more vigorously supplied deeply-sourced Si in the low-latitude or subarctic Atlantic
448 (Fig. 9), allowing it to produce NADW with a high $\delta^{30}\text{Si}$ value. Conversely, the more adiabatic models
449 P2A and LL favour distal control on the elevated $\delta^{30}\text{Si}$ of NADW. The models thus trade off between
450 distal and proximal isotope fractionation as a means of supplying isotopically fractionated Si to the
451 NADW formation region. It is this compensation that allows all three models to produce Atlantic $\delta^{30}\text{Si}$
452 systematics that are remarkably similar to observations (Fig. 1a), despite their widely-varying MOC
453 pathways. The existence of these interacting controls on the NADW $\delta^{30}\text{Si}$ signature also means that
454 the presence of an Atlantic $\delta^{30}\text{Si}$ gradient cannot be uniquely tied to fractionation in the high-latitude

455 Southern Ocean, as suggested by de Souza et al. (2012a). As a result, our simulations indicate that this
456 isotopic feature does not constrain the pathways by which deep water is returned to the upper ocean in
457 the MOC.

458 More generally, the results of our study contribute to an emerging picture of the role of Southern
459 Ocean Si isotope “distillation” (Brzezinski and Jones, 2015) in governing the marine $\delta^{30}\text{Si}$ distribution.
460 This distillation results from the combined physical and biogeochemical dynamics of the Southern
461 Ocean, and leads to the trapping of low- $\delta^{30}\text{Si}$ silicic acid in the deep Southern Ocean (Holzer et al.,
462 2014; Holzer and Brzezinski, 2015) coupled to a complementary northward export of a high- $\delta^{30}\text{Si}$
463 signature in SAMW/AAIW (Fripiat et al., 2011; de Souza et al., 2012b). de Souza et al. (2014) have
464 recently shown that the isotopically light preformed and regenerated Si in the deep Southern Ocean is
465 spread throughout the global abyssal ocean by AABW, producing the observed hydrographic control
466 on the deep $\delta^{30}\text{Si}$ distribution. This study has highlighted the large-scale influence of the
467 complementary high $\delta^{30}\text{Si}$ signal exported in SAMW/AAIW, showing that the Southern Ocean
468 influences the global $\delta^{30}\text{Si}$ distribution by two separate pathways associated with the upper *and* lower
469 limbs of the MOC. However, consistent with the recent study by Holzer and Brzezinski (2015), our
470 results also allow a role for fractionation during low-latitude Si cycling in determining the large-scale
471 $\delta^{30}\text{Si}$ distribution, indicating that other ocean regions may modulate the signals exported from the
472 Southern Ocean.

473 An important open question that our study does not explicitly address is the role of the Arctic
474 Ocean, which Brzezinski and Jones (2015) have suggested may represent an important northern
475 counterpart to the Southern Ocean, via its influence on the Nordic Sea overflows. The Arctic Ocean
476 receives fractionated Si primarily through shallow inflow from the North Atlantic, and transfers this Si
477 to deep-water densities via buoyancy loss (Jones et al., 1995). Certainly some of the SAMW/AAIW-
478 sourced Si in our models’ NADW has been incorporated in this manner. What remains to be assessed
479 is whether the Arctic Ocean’s role is limited to such diapycnal Si transfer, or whether a significant
480 additional fractionation signal is imposed by Si cycling within the Arctic itself. Answering this
481 question will require the long-overdue analysis of the Arctic $\delta^{30}\text{Si}$ distribution.

482

483 **5. Conclusions**

484 This study has combined models of the marine cycle of Si and its isotopes with a diagnostic scheme
485 that enables us to trace the large-scale transport of Si originating from the high-latitude ocean in a
486 suite of OGCM simulations with varying MOC pathways. These simulations allow an assessment of
487 the role of cross-equatorial transport of SAMW- and AAIW-derived Si in producing the elevated $\delta^{30}\text{Si}$
488 signature of NADW. We find that Si sourced from the SAMW and AAIW formation regions
489 contributes a major to dominant fraction (46-62%) of the freshly-ventilated NADW Si inventory
490 irrespective of MOC pathway, and that the $\delta^{30}\text{Si}$ signature of NADW rises as the contribution of
491 SAMW- and AAIW-derived Si increases. However, the simulations also indicate that more proximal
492 isotope fractionation of Si, within the low-latitude or subpolar North Atlantic, can influence the
493 NADW $\delta^{30}\text{Si}$ signature. By revealing this interplay between distal and proximal processes, our results
494 thus allow us to refine the hypothesis of de Souza et al. (2012a): the high $\delta^{30}\text{Si}$ signature of NADW is
495 vitally linked to the transport of a fractionated signal from the surface Southern Ocean by
496 SAMW/AAIW, but may also be additionally influenced by Si isotope fractionation that takes place
497 during transport to the NADW formation region. The more adiabatic models in our suite, which
498 conform best to our current understanding of deep-water upwelling pathways (e.g. Talley, 2013),
499 suggest that the proximal contribution is small, although definitive conclusions remain elusive given
500 lingering uncertainties regarding the pathways of the MOC (e.g. Talley, 2008).

501

502 **Acknowledgements**

503 The authors gratefully acknowledge helpful comments on an earlier version of this manuscript by
504 Timothy Conway and Beatrice Radden Keefe, and the constructive reviews of two anonymous
505 reviewers. This work was supported by Swiss National Science Foundation post-doctoral fellowships
506 PBEZP2-140169 and P300P2-147747 granted to GFDS, NOAA grant NA11OAR4310066 to JLS, and
507 UK NERC grant NE/K00901X/1 to MPH.

508

509 **References**

- 510 Abouchami, W., Galer, S. J. G., de Baar, H. J. W., Middag, R., Vance, D., Zhao, Y., et al., 2014.
511 Biogeochemical cycling of cadmium isotopes in the Southern Ocean along the Zero Meridian.
512 *Geochim. Cosmochim. Acta* 127, 348-367.
- 513 Broecker, W. S., Peng, T. H., 1982. *Tracers In The Sea*. Eldigio Press/Lamont-Doherty Geological
514 Observatory, Palisades, NY.
- 515 Broecker, W.S., Blanton, S., Smethie, W.M., Ostlund, G., 1991. Radiocarbon decay and oxygen
516 utilization in the deep Atlantic Ocean. *Glob. Biogeochem. Cyc.* 5, 87-117.
- 517 Brzezinski, M. A., Dickson, M. L., Nelson, D. M., Sambrotto, R., 2003. Ratios of Si, C and N uptake
518 by microplankton in the Southern Ocean. *Deep-Sea Res. II* 50, 619-633.
- 519 Brzezinski, M. A., Jones, J. L., 2015. Coupling of the distribution of silicon isotopes to the meridional
520 overturning circulation of the North Atlantic Ocean. *Deep Sea Res. II* 116, 79-88.
- 521 Buesseler, K. O., 1998. The decoupling of production and particulate export in the surface ocean.
522 *Glob. Biogeochem. Cyc.* 12, 297-310.
- 523 Cardinal, D., Alleman, L. Y., Dehairs, F., Savoye, N., Trull, T. W., Andre, L., 2005. Relevance of
524 silicon isotopes to Si-nutrient utilization and Si-source assessment in Antarctic waters. *Glob.*
525 *Biogeochem. Cyc.* 19, doi: 10.1029/2004GB002364.
- 526 De La Rocha, C. L., Brzezinski, M. A., DeNiro, M. J., 1997. Fractionation of silicon isotopes by
527 marine diatoms during biogenic silica formation. *Geochim. Cosmochim. Acta* 61, 5051-5056.
- 528 Demarest, M. S., Brzezinski, M. A., Beucher, C. P., 2009. Fractionation of silicon isotopes during
529 biogenic silica dissolution. *Geochim. Cosmochim. Acta* 73, 5572-5583.
- 530 de Souza, G. F., Reynolds, B. C., Rickli, J., Frank, M., Saito, M. A., Gerringa, L. J. A., et al., 2012a.
531 Southern Ocean control of silicon stable isotope distribution in the deep Atlantic Ocean. *Glob.*
532 *Biogeochem. Cyc.* 26, doi: 10.1029/2011gb004141.
- 533 de Souza, G. F., Reynolds, B. C., Johnson, G. C., Bullister, J. L., Bourdon, B., 2012b. Silicon stable
534 isotope distribution traces Southern Ocean export of Si to the eastern South Pacific thermocline.
535 *Biogeosci.* 9, 4199-4213.

536 de Souza, G. F., Slater, R. D., Dunne, J. P., Sarmiento, J. L., 2014. Deconvolving the controls on the
537 deep ocean's silicon stable isotope distribution. *Earth Planet. Sci. Lett.* 398, 66-76.

538 Fripiat, F., Cavagna, A.-J., Dehairs, F., Speich, S., André, L., Cardinal, D., 2011. Silicon pool
539 dynamics and biogenic silica export in the Southern Ocean, inferred from Si-isotopes. *Ocean Sci.* 7,
540 533-547.

541 Garcia, H. E., Locarnini, R. A., Boyer, T. P., Antonov, J. I., 2010. *World Ocean Atlas 2009, Volume 4:*
542 *Nutrients (phosphate, nitrate, silicate)*. U.S. Government Printing Office, Washington DC.

543 Gent, P. R., Willebrand, J., McDougall, T. J., McWilliams, J. C., 1995. Parametrizing eddy-induced
544 tracer transports in ocean circulation models. *J. Phys. Oceanogr.* 25, 463-474.

545 Gnanadesikan, A., 1999. A simple predictive model for the structure of the oceanic pycnocline.
546 *Science* 283, 2077-2079.

547 Gnanadesikan, A., Slater, R. D., Gruber, N., Sarmiento, J. L., 2002. Oceanic vertical exchange and
548 new production: a comparison between models and observations. *Deep Sea Res. II* 49, 363-401.

549 Gnanadesikan, A., Dunne, J., Key, R., Matsumoto, K., Sarmiento, J. L., Slater, R., et al., 2004.
550 Oceanic ventilation and biogeochemical cycling: Understanding the physical mechanisms that
551 produce realistic distributions of tracers and productivity. *Glob. Biogeochem. Cyc.* 18, doi:
552 10.1029/2003GB002097.

553 Gnanadesikan, A., De Boer, A. M., Mignone, B. K., 2007. A simple theory of the pycnocline and
554 overturning revisited. In: Schmittner, A., Chiang, J. C. H., and Hemming, S., (Eds.), *Ocean*
555 *Circulation: Mechanisms and Impacts—Past and Future Changes of Meridional Overturning*.
556 American Geophysical Union, pp 19-32.

557 Gordon, A. L., 1986. Interocean exchange of thermocline water. *J. Geophys. Res. Ocean.* 91, 5037-
558 5046.

559 Grasse, P., Ehlert, C., Frank, M., 2013. The influence of water mass mixing on the dissolved Si
560 isotope composition in the Eastern Equatorial Pacific. *Earth Planet. Sci. Lett.* 380, 60-71.

561 Hain, M. P. Sigman, D. M, Haug, G. H., 2014a. The biological pump in the past, in: Holland, H. and
562 Turekian, K. K. (Eds.), *Treatise on Geochemistry*, second ed. Elsevier, Amsterdam, pp. 485-517.

563 Hain, M. P., Sigman, D. M., Haug, G. H., 2014b. Distinct roles of the Southern Ocean and North
564 Atlantic in the deglacial atmospheric radiocarbon decline. *Earth Planet. Sci. Lett.* 394, 198-208.

565 Hellerman, S., Rosenstein, M., 1983. Normal monthly wind stress over the world ocean with error
566 estimates. *J. Phys. Oceanogr.* 13, 1093-1104.

567 Holzer, M., Primeau, F. W., DeVries, T., Matear, R., 2014. The Southern Ocean silicon trap: data-
568 constrained estimates of regenerated silicic acid, trapping efficiencies, and global transport paths. *J.*
569 *Geophys. Res. Ocean.* 119, doi: 10.1002/2013jc009356.

570 Holzer, M., Brzezinski, M. A., 2015. Controls on the silicon isotope distribution in the ocean: new
571 diagnostics from a data-constrained model. *Glob. Biogeochem. Cyc.* 29, doi:
572 10.1002/2014GB004967.

573 Jin, X., Gruber, N., Dunne, J. P., Sarmiento, J. L., Armstrong, R. A., 2006. Diagnosing the
574 contribution of phytoplankton functional groups to the production and export of particulate organic
575 carbon, CaCO₃, and opal from global nutrient and alkalinity distributions. *Glob. Biogeochem. Cyc.*
576 20, doi: 10.1029/2005GB002532.

577 Jones, E. P., Rudels, B., Anderson, L. G., 1995. Deep waters of the Arctic Ocean: origins and
578 circulation. *Deep Sea Res. I* 42, 737-760.

579 Karleskind, P., Lévy, M., Memery, L., 2011. Subduction of carbon, nitrogen, and oxygen in the
580 northeast Atlantic. *J. Geophys. Res. Ocean.* 116, doi: 10.1029/2010jc006446.

581 Keir, R. S., 1988. On the Late Pleistocene ocean geochemistry and circulation. *Paleoceanogr.* 3, 413-
582 455.

583 Ledwell, J. R., Watson, A. J., Law, C. S., 1993. Evidence for slow mixing across the pycnocline from
584 an open-ocean tracer-release experiment. *Nature* 364, 701-703.

585 Ledwell, J. R., Watson, A. J., Law, C. S., 1998. Mixing of a tracer in the pycnocline. *J. Geophys. Res.*
586 *Ocean.* 103, 21,499–21,529.

587 Lumpkin, R., Speer, K., 2007. Global ocean meridional overturning. *J. Phys. Oceanogr.* 37, 2550-
588 2562.

589 Marinov, I., Gnanadesikan, A., Toggweiler, J. R., Sarmiento, J. L., 2006. The Southern Ocean
590 biogeochemical divide. *Nature* 441, 964-967.

591 Marshall, J., Speer, K., 2012. Closure of the meridional overturning circulation through Southern
592 Ocean upwelling. *Nature Geosci.* 5, 171-180.

593 Matsumoto, K., Sarmiento, J. L., Key, R. M., Aumont, O., Bullister, J. L., Caldeira, K., et al., 2004.
594 Evaluation of ocean carbon cycle models with data-based metrics. *Geophys. Res. Lett.* 31, doi:
595 10.1029/2003gl018970.

596 Morrison, A.K., Fröhlicher, T.L., Sarmiento, J.L., 2015. Upwelling in the Southern Ocean. *Physics*
597 *Today* 68, doi: 10.1063/PT.1063.2654.

598 Pacanowski, R. C., Griffies, S. M., 1999. *The MOM3.0 Manual*, NOAA/Geophysical Fluid Dynamics
599 Laboratory, Princeton.

600 Palter, J. B., Lozier, M. S., Barber, R. T., 2005. The effect of advection on the nutrient reservoir in the
601 North Atlantic subtropical gyre. *Nature* 437, 687-692.

602 Palter, J. B., Sarmiento, J. L., Gnanadesikan, A., Simeon, J., Slater, R. D., 2010. Fueling export
603 production: nutrient return pathways from the deep ocean and their dependence on the meridional
604 overturning circulation. *Biogeosci.* 7, 3549-3568.

605 Palter, J. B., Lozier, M. S., Sarmiento, J. L., Williams, R. G., 2011. The supply of excess phosphate
606 across the Gulf Stream and the maintenance of subtropical nitrogen fixation. *Glob. Biogeochem.*
607 *Cyc.* 25, doi: 10.1029/2010GB003955.

608 Polzin, K. L., Toole, J. M., Ledwell, J. R., Schmitt, R. W., 1997. Spatial variability of turbulent mixing
609 in the abyssal ocean. *Science* 276, 93-96.

610 Raven, J. A., 1983. The transport and function of silicon in plants. *Biol. Rev.* 58, 179-207.

611 Reynolds, B. C., Frank, M., Halliday, A. N., 2006. Silicon isotope fractionation during nutrient
612 utilization in the North Pacific. *Earth Planet. Sci. Lett.* 244, 431-443.

613 Robinson, A., Stommel, H., 1959. The oceanic thermocline and the associated thermohaline
614 circulation. *Tellus* 11, 295-308.

615 Robinson, R. S., Sigman, D. M., DiFiore, P. J., Rohde, M. M., Mashiotta, T. A., Lea, D. W., 2005.
616 Diatom-bound $^{15}\text{N}/^{14}\text{N}$: new support for enhanced nutrient consumption in the ice age Subantarctic.
617 *Paleoceanogr.* 20, doi: 10.1029/2004pa001114.

618 Sarmiento, J. L., Gruber, N., Brzezinski, M. A., Dunne, J. P., 2004. High-latitude controls of
619 thermocline nutrients and low latitude biological productivity. *Nature* 427, 56-60.

620 Sarmiento, J. L., Simeon, J., Gnanadesikan, A., Gruber, N., Key, R. M., Schlitzer, R., 2007. Deep
621 ocean biogeochemistry of silicic acid and nitrate. *Glob. Biogeochem. Cyc.* 21,
622 doi:10.1029/2006GB002720.

623 Sallée, J.-B., Speer, K., Rintoul, S., Wijffels, S., 2010. Southern Ocean thermocline ventilation. *J.*
624 *Phys. Oceanogr.* 40, 509-529.

625 Sigman, D. M., Altabet, M. A., McCorkle, D. C., François, R., Fischer, G., 2000. The $\delta^{15}\text{N}$ of nitrate
626 in the Southern Ocean: nitrogen cycling and circulation in the ocean interior. *J. Geophys. Res.*
627 *Ocean.* 105, 19599-19614.

628 Smetacek, V., 1999. Diatoms and the ocean carbon cycle. *Protist* 150, 25-32.

629 Sutton, J. N., Varela, D. E., Brzezinski, M. A., Beucher, C. P., 2013. Species-dependent silicon isotope
630 fractionation by marine diatoms. *Geochim. Cosmochim. Acta* 104, 300-309.

631 Talley, L. D., 2008. Freshwater transport estimates and the global overturning circulation: Shallow,
632 deep and throughflow components. *Prog. Oceanogr.* 78, 257-303.

633 Talley, L. D., 2013. Closure of the global overturning circulation through the Indian, Pacific, and
634 Southern Oceans: schematics and transports. *Oceanogr.* 26, 80-97.

635 Talley, L. D., Reid, J. L., Robbins, P. E., 2003. Data-based meridional overturning streamfunctions for
636 the global ocean. *J. Clim.* 16, 3213-3226.

637 Toggweiler, J. R., Samuels, B., 1993. New radiocarbon constraints on the upwelling of abyssal water
638 to the ocean's surface, in: Heimann, M., (Ed.), *The Global Carbon Cycle*. Springer, Berlin, pp. 333-
639 366.

640 Tréguer, P. J., De La Rocha, C. L., 2013. The world ocean silica cycle. *Ann. Rev. Mar. Sci.* 5, 477-
641 501.

642 Trenberth, K. E., Olson, J., Large, W., 1989. *A global ocean wind stress climatology based on*
643 *ECMWF analyses*. Technical Report NCAR/TN-338+STR, National Center for Atmospheric
644 Research, Boulder, CO.

645 Wetzel, F., de Souza, G. F., Reynolds, B. C., 2014. What controls silicon isotope fractionation during
646 dissolution of diatom opal? *Geochim. Cosmochim. Acta* 131, 128-137.
647

648 **Table 1: Quantification of Si source contributions to freshly-ventilated NADW. Threshold values**
649 **of $\Delta^{14}\text{C}$ and $[\text{O}_2]$ used to define the volume of freshly-ventilated North Atlantic Deep Water (see**
650 **Supplementary Information) in the model variants used in this study, together with integrated**
651 **$\delta^{30}\text{Si}$ signature and contributions of the four source regions to the Si inventory of this volume.**

	HH	LL	P2A
Radiocarbon threshold [‰]	-70	-70	-80
Oxygen threshold [mmol/m ³]	260	260	240
<i>Properties of the NADW volume:</i>			
NADW $\delta^{30}\text{Si}$ [‰]	+1.50	+1.66	+1.74
<i>f</i> (SAMW)	0.166	0.124	0.267
<i>f</i> (AAIW)	0.292	0.368	0.348
<i>f</i>(SAMW+AAIW)	0.457	0.491	0.615
<i>f</i> (DEEP)	0.484	0.419	0.331
<i>f</i> (NPAC)	0.059	0.090	0.054
<i>Source-region isotope signatures:</i>			
SAMW $\delta^{30}\text{Si}$ [‰]	+1.71	+2.07	+2.31
AAIW $\delta^{30}\text{Si}$ [‰]	+1.37	+1.47	+1.52
DEEP $\delta^{30}\text{Si}$ [‰]	+1.19	+1.18	+1.15
NPAC $\delta^{30}\text{Si}$ [‰]	+1.62	+1.66	+1.57
<i>Source-region signature propagation (Eqn. 1):</i>			
NADW $\delta^{30}\text{Si}_{\text{distal}}$ [‰]	+1.35	+1.44	+1.61
NADW $\delta^{30}\text{Si}_{\text{distal}}$ – NADW $\delta^{30}\text{Si}$ [‰]	–0.14	–0.22	–0.13
<i>Deep Atlantic $\delta^{30}\text{Si}$ gradient:</i>			
AABW $\delta^{30}\text{Si}$ [‰]	+1.18	+1.16	+1.10
NADW $\delta^{30}\text{Si}$ – AABW $\delta^{30}\text{Si}$ [‰]	0.31	0.50	0.64
NADW $\delta^{30}\text{Si}_{\text{distal}}$ – AABW $\delta^{30}\text{Si}$ [‰]	0.17	0.28	0.51
Fraction of $\delta^{30}\text{Si}$ difference explained by $\delta^{30}\text{Si}_{\text{distal}}$	54%	56%	80%

652

653 **FIGURE CAPTIONS**

654

655 **Fig. 1:** Silicon isotope data from the Atlantic Ocean. (a) Data from the deep (>2000m) Atlantic Ocean
656 from latitudes ranging from ~60°N to ~60°S in isotope mixing space (de Souza et al., 2012a),
657 illustrating the systematic variation of deep water $\delta^{30}\text{Si}$ values. The near-linear relationship between
658 $\delta^{30}\text{Si}$ and $1/[\text{Si}]$ indicates quasi-conservative mixing of Si brought into the deep Atlantic by Si-rich
659 Southern Ocean sources (CDW) as well as Si-poor North Atlantic (LSW) and Nordic (DSOW, ISOW)
660 sources. Open red symbols are results from the OGCMs used in this study (see Section 2.1),
661 subsampled at the observational sampling locations. (b) Depth profiles of $\delta^{30}\text{Si}$ from the
662 GEOTRACES North Atlantic Zonal Transect at 20°–40°N (Brzezinski and Jones, 2015) reveal the
663 elevated $\delta^{30}\text{Si}$ values associated with the southward transport of NADW at mid-depths in the western
664 Atlantic Ocean (blue and green points; see inset).

665

666 **Fig. 2:** (a) Schematic representation of the Atlantic circulation in the CYCLOPS ocean box model
667 (Hain et al., 2014b), highlighting advective transport (black arrows) and diffusive exchange (red
668 arrows) fluxes. In the sensitivity study discussed in the text (Section 1.2), the Si concentration of the
669 Subantarctic surface box (light red shading) was systematically varied together with the length scale of
670 opal dissolution, which controls the fraction of the sinking opal flux exported to the deep ocean boxes.
671 The results of these parameter variations on the deep Atlantic $[\text{Si}]$ and $\delta^{30}\text{Si}$ gradients (calculated as
672 the difference between the deep high-latitude boxes; light blue shading) is shown in panel *b* (warm
673 colours: $\Delta[\text{Si}]$ in μM ; cool colours: $\Delta\delta^{30}\text{Si}$ in ‰). PAZ: polar Antarctic zone; AZ: Antarctic zone. The
674 light blue shaded region in panel *b* corresponds to observations ($\Delta[\text{Si}] \sim 108 \mu\text{M}$, $\Delta\delta^{30}\text{Si} \sim 0.5\text{‰}$).

675

676 **Fig. 3:** (a) Theoretical model framework of Gnanadesikan (1999) and (b) northward meridional
677 volume transport above the $\sigma_\theta = 27.4$ isopycnal in the suite of OGCMs used in this study, whose
678 construction is based on the theory of Gnanadesikan (1999). In panel *a*, the depth D of the pycnocline
679 (light blue shading) is maintained by the volume balance between flux T_n representing sinking of

680 dense water in the North Atlantic, T_u representing low-latitude upwelling, and the balance between
681 wind-driven northward Ekman transport T_w and eddy-induced southward transport T_e in the Southern
682 Ocean.

683

684 **Fig. 4:** Schematic meridional Atlantic section showing the tagging scheme employed to trace Si
685 sources to the North Atlantic Ocean. Curved black lines represent potential density anomaly (σ_θ)
686 surfaces labeled at their southern outcrop. Each coloured area represents a tagging region within which
687 Si is assigned a source “identity”. Four sources of Si are traced: SAMW, AAIW, deep Southern Ocean
688 (*DEEP*) and North Pacific (*NPAC*). The southern hemisphere tagging regions are circumpolar, whilst
689 the NPAC tagging region is restricted to the North Pacific Ocean. The identity of Si tagged in any one
690 region is destroyed when it enters another coloured tagging region, where it is assigned a new source
691 identity. Within the grey area, tagged Si is cycled by biology and transported by the physical
692 circulation analogously to the total Si pool.

693

694 **Fig. 5:** Meridional sections showing the Atlantic-mean Si distribution in the uppermost 2400m in
695 World Ocean Atlas 2009 (upper left) and the three model variants. Concentrations are averaged over
696 the Atlantic basin, and over the Southern Ocean from 60°W to 30°E.

697

698 **Fig. 6:** Contribution of each source region to the Si inventory of the thermocline ($\sigma_\theta < 26.8$) in the three
699 model variants [mol Si/mol Si, unitless]. White shading indicates the absence of water lighter than
700 $\sigma_\theta = 26.8$.

701

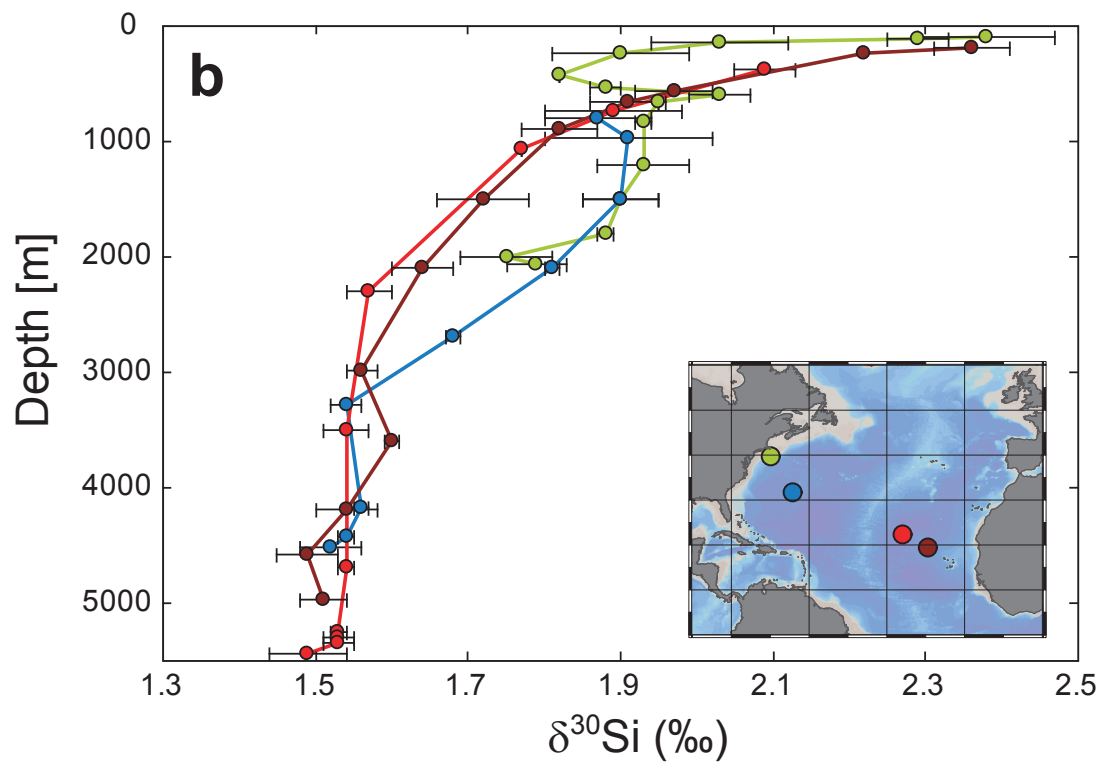
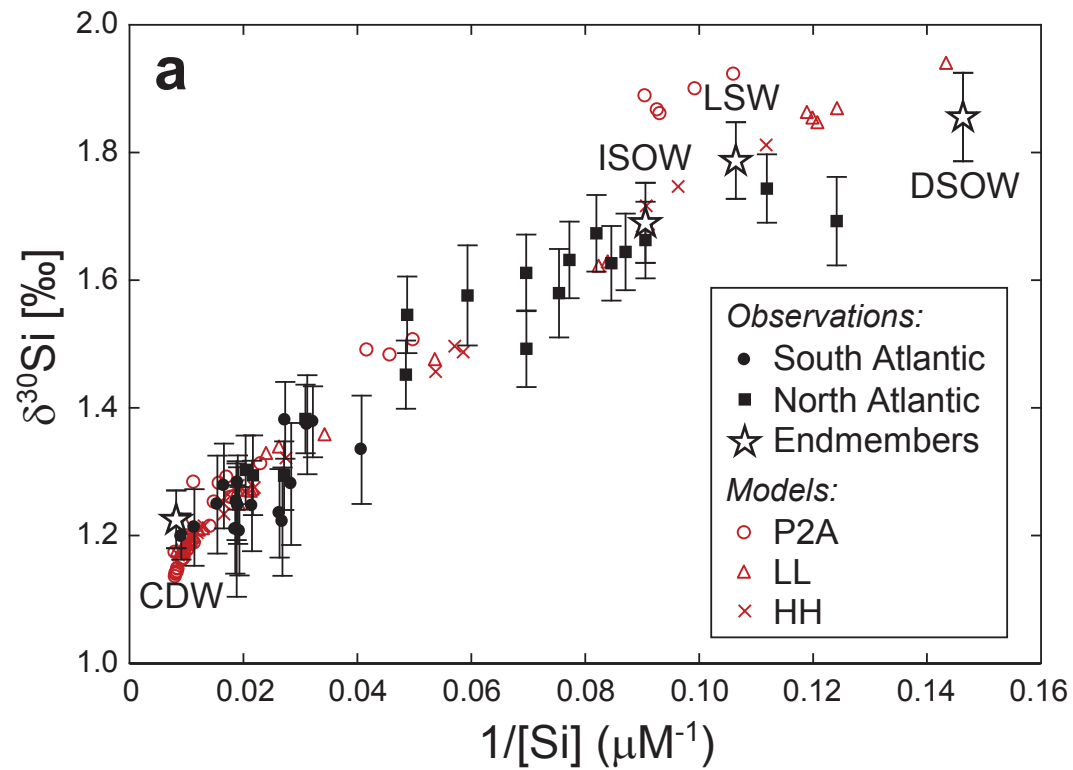
702 **Fig. 7:** Meridional section showing the Atlantic-mean contribution of the four source regions to the Si
703 inventory [mol Si/mol Si, unitless] in the uppermost 2400m of the three model variants. The three
704 white contours correspond to the density horizons used to determine the tagging regions for SAMW-
705 and AAIW-sourced Si (Fig. 4). Fractions are averaged over the Atlantic basin and over the Southern
706 Ocean from 60°W to 30°E.

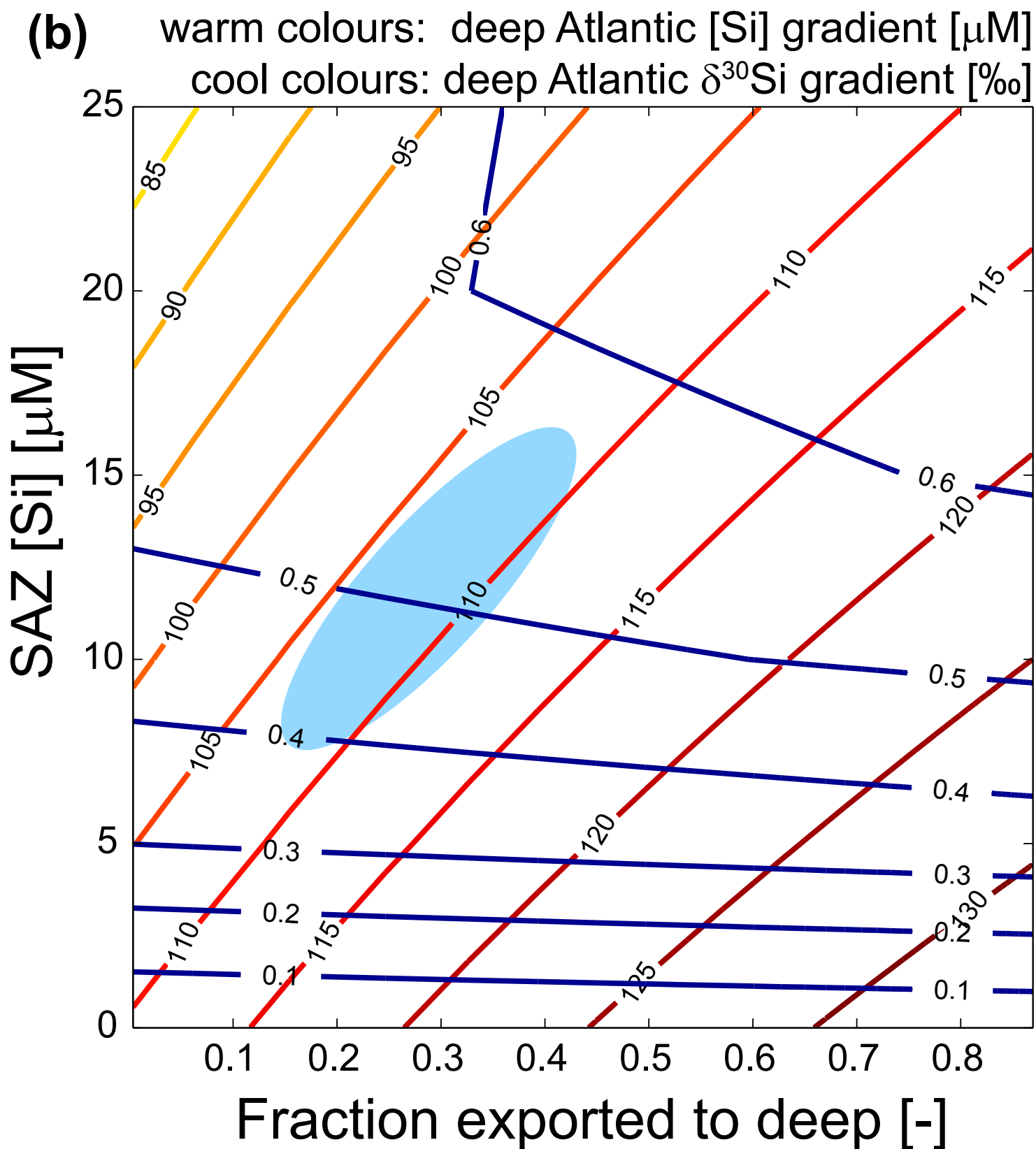
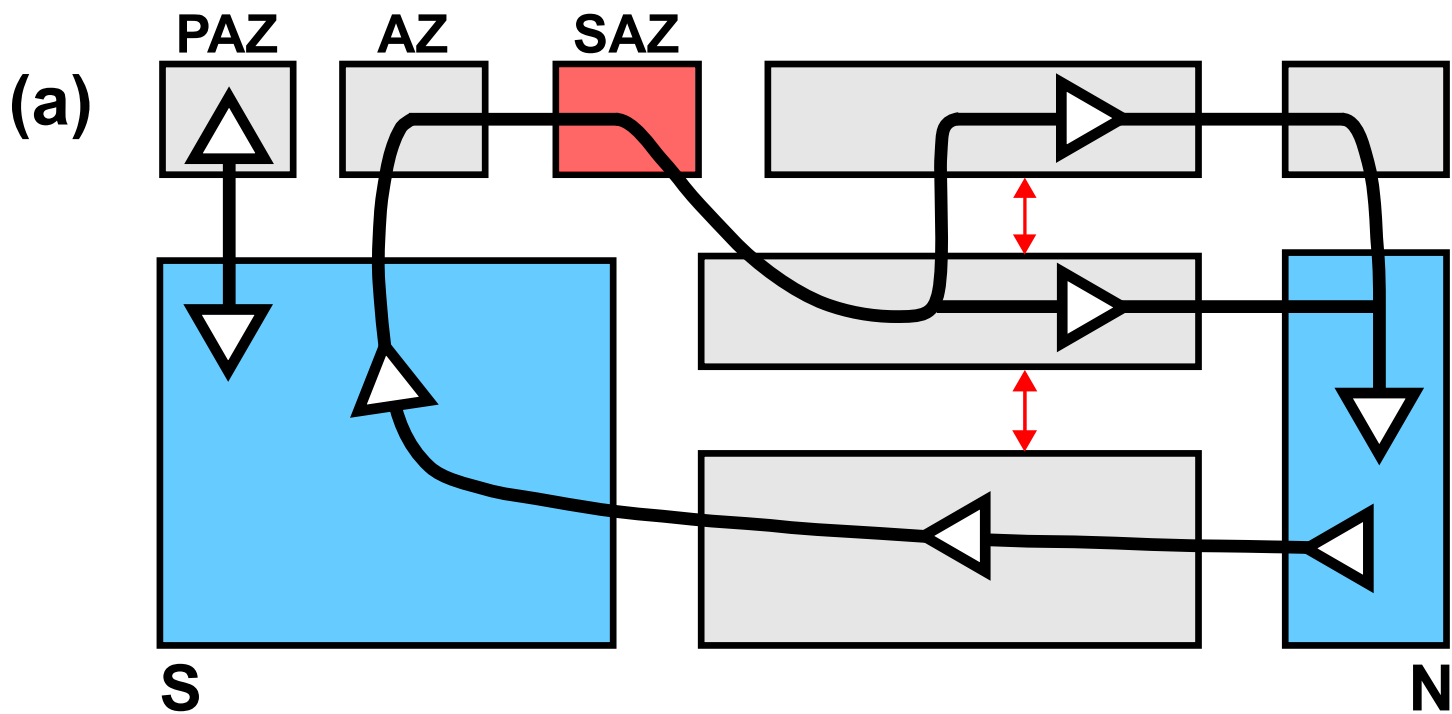
707

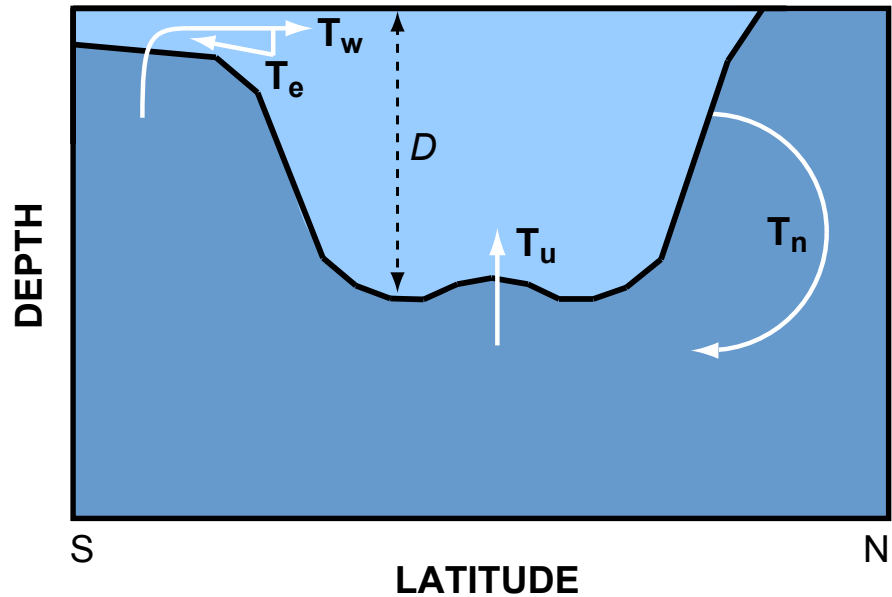
708 **Fig. 8:** Isotopic signatures and source composition of NADW in the North Atlantic Ocean. (a)
709 Distribution of $\delta^{30}\text{Si}$ at ~1700m water depth, illustrating the southward spreading of the high- $\delta^{30}\text{Si}$
710 signature of NADW as a deep western boundary current. The white dotted line at ~43°N in column *a*
711 marks the latitude of the depth sections in columns *b–d*, which show (b) the pre-industrial $\Delta^{14}\text{C}$
712 distribution (‰), (c) the $\delta^{30}\text{Si}$ distribution (‰), and (d) the fractional contribution of SAMW- and
713 AAIW-derived Si to the Si inventory (mol Si/mol Si, unitless).

714

715 **Fig. 9:** Meridional sections at 25°W in the Atlantic Ocean from all three model variants, comparing (a)
716 the simulated $\delta^{30}\text{Si}$ distribution with (b) the $\delta^{30}\text{Si}_{\text{distal}}$ distribution calculated using Eqn. 1, i.e. the $\delta^{30}\text{Si}$
717 distribution expected simply from propagation of source-region $\delta^{30}\text{Si}$ signatures. Panel *c* shows the
718 difference between panels *a* and *b*. White solid lines are isopycnal surfaces used in the definition of
719 SAMW and AAIW tagging regions (Fig. 4); the white dotted line marks 30°S, the northernmost extent
720 of the DEEP tagging region. In panel *d*, a scatterplot directly compares the deep $\delta^{30}\text{Si}_{\text{distal}}$ distribution
721 (> 1000 m) to the simulated $\delta^{30}\text{Si}$ distribution north of 30°S, illustrating both the clear correlation
722 between the two fields as well as the muted dynamic range of $\delta^{30}\text{Si}_{\text{distal}}$.





(a)**(b)**